PROCEEDINGS OF SPIE

Infrared Technology and Applications XL

Bjørn F. Andresen
Gabor F. Fulop
Charles M. Hanson
Paul R. Norton
Editors

5–8 May 2014
Baltimore, Maryland, United States

Sponsored and Published by
SPIE

Volume 9070
Part One of Two Parts

Proceedings of SPIE 0277-786X, V. 9070

Infrared Technology and Applications XL, edited by Bjørn F. Andresen, Gabor F. Fulop, Charles M. Hanson, Paul R. Norton, Proc. of SPIE Vol. 9070, 907001 · © 2014 SPIE
CCC code: 0277-786X/14/$18 · doi: 10.1117/12.2073306

The papers included in this volume were part of the technical conference cited on the cover and title page. Papers were selected and subject to review by the editors and conference program committee. Some conference presentations may not be available for publication. The papers published in these proceedings reflect the work and thoughts of the authors and are published herein as submitted. The publisher is not responsible for the validity of the information or for any outcomes resulting from reliance thereon.

Please use the following format to cite material from this book:
Author(s), "Title of Paper," in *Infrared Technology and Applications XL*, edited by
Bjørn F. Andresen, Gabor F. Fulop, Charles M. Hanson, Paul R. Norton, Proceedings of SPIE Vol. 9070 (SPIE, Bellingham, WA, 2014) Article CID Number.

ISSN: 0277-786X
ISBN: 9781628410075

Published by
SPIE
P.O. Box 10, Bellingham, Washington 98227-0010 USA
Telephone +1 360 676 3290 (Pacific Time) · Fax +1 360 647 1445
SPIE.org

Printed in the United States of America.

Publication of record for individual papers is online in the SPIE Digital Library.

SPIEDigitalLibrary.org

Paper Numbering: Proceedings of SPIE follow an e-First publication model, with papers published first online and then in print and on CD-ROM. Papers are published as they are submitted and meet publication criteria. A unique, consistent, permanent citation identifier (CID) number is assigned to each article at the time of the first publication. Utilization of CIDs allows articles to be fully citable as soon as they are published online, and connects the same identifier to all online, print, and electronic versions of the publication. SPIE uses a six-digit CID article numbering system in which:

- The first four digits correspond to the SPIE volume number.
- The last two digits indicate publication order within the volume using a Base 36 numbering system employing both numerals and letters. These two-number sets start with 00, 01, 02, 03, 04, 05, 06, 07, 08, 09, 0A, 0B … 0Z, followed by 10-1Z, 20-2Z, etc.

The CID Number appears on each page of the manuscript. The complete citation is used on the first page, and an abbreviated version on subsequent pages. Numbers in the index correspond to the last two digits of the six-digit CID Number.

Contents

ADVANCES IN OPTICAL AND DETECTOR MATERIALS

HOT: HIGH OPERATING TEMPERATURE FPAS

UNCOOLED FPAS AND APPLICATIONS

Part 2

EMERGING UNCOOLED TECHNOLOGIES

IR OPTICS II: BREAKTHROUGHS IN MULTIBAND MOLDABLE GLASSES

IR OPTICS III: MULTIBAND IR-GRIN LENSES

EMERGING CRYOGENIC COOLERS

CRYOGENIC COOLERS

HgCdTe

SMART PROCESSING

FACE RECOGNITION

Conference Committee

Symposium Chair

David A. Whelan, Boeing Defense, Space, and Security (United States)

Symposium Co-chair

Nils R. Sandell Jr., Strategic Technology Office, DARPA (United States)

Conference Chairs

Bjørn F. Andresen, Senso Optics Ltd. (Israel)
Gabor F. Fulop, Maxtech International, Inc. (United States)
Charles M. Hanson, Texas Instruments Inc. (United States)
Paul R. Norton, U.S. Army Night Vision & Electronic Sensors Directorate (United States)

Conference Program Committee

Tayfun Akin, Mikro-Tasarim Ltd. (Turkey) and Middle East Technical University (Turkey)
Christopher C. Alexay, StingRay Optics, LLC (United States)
Jagmohan Bajaj, Teledyne Imaging Sensors (United States)
Stefan T. Baur, Raytheon Vision Systems (United States)
Philippe F. Bois, Thales Research & Technology (France)
Wolfgang A. Cabanski, AIM INFRAROT-MODULE GmbH (Germany)
John T. Caulfield, Cyan Systems (United States)
Eric M. Costard, SOFRADIR (France)
Nibir K. Dhar, Defense Advanced Research Projects Agency (United States)
Michael T. Eismann, Air Force Research Laboratory (United States)
Mark E. Greiner, L-3 Communications Cincinnati Electronics (United States)
Sarath D. Gunapala, Jet Propulsion Laboratory (United States)
Andrew Hood, FLIR Electro-Optical Components (United States)
Masafumi Kimata, Ritsumeikan University (Japan)
Hee Chul Lee, KAIST (Korea, Republic of)
Paul D. LeVan, Air Force Research Laboratory (United States)
Chuan C. Li, DRS Technologies, Inc. (United States)
Kevin C. Liddiard, Electro-optic Sensor Design (Australia)
Wei Lu, Shanghai Institute of Technical Physics (China)
Tara J. Martin, UTC Aerospace Systems (United States)
Paul L. McCarley, Air Force Research Laboratory (United States)
R. Kennedy McEwen, SELEX ES (United Kingdom)

John L. Miller, FLIR Systems, Inc. (United States)
A. Fenner Milton, U.S. Army Night Vision & Electronic Sensors Directorate (United States)
Mario O. Münzberg, Cassidian Optronics GmbH (Germany)
Peter W. Norton, BAE Systems (United States)
Robert A. Owen, L-3 Communications Infrared Products (United States)
Joseph G. Pellegrino, U.S. Army Night Vision & Electronic Sensors Directorate (United States)
Manijeh Razeghi, Northwestern University (United States)
Colin E. Reese, U.S. Army Night Vision & Electronic Sensors Directorate (United States)
Ingmar G. Renhorn, Swedish Defense Research Agency (Sweden)
Patrick Robert, ULIS (France)
Antoni Rogalski, Military University of Technology (Poland)
Ingo Rühlich, AIM INFRAROT-MODULE GmbH (Germany)
Piet B. W. Schwering, TNO Defence, Security and Safety (Netherlands)
Itay Shtrichman, SCD Semiconductor Devices (Israel)
Rengarajan Sudharsanan, Spectrolab, Inc., A Boeing Company (United States)
Stefan P. Svensson, U.S. Army Research Laboratory (United States)
Venkataraman Swaminathan, U.S. Army Armament Research, Development and Engineering Center (United States)
J. Ralph Teague, Georgia Tech Research Institute (United States)
Simon Thibault, Université Laval (Canada)
Gil A. Tidhar, Israel Aerospace Industries-Elta Systems Ltd. (Israel)
Meimei Tidrow, U.S. Army Night Vision & Electronic Sensors Directorate (United States)
Alexander Veprik, SCD Semiconductor Devices (Israel)
Jay N. Vizgaitis, U.S. Army Night Vision & Electronic Sensors Directorate (United States)
Michel Vuillermet, SOFRADIR (France)
James R. Waterman, U.S. Naval Research Laboratory (United States)
Lucy Zheng, Institute for Defense Analyses (United States)

Session Chairs

1 NIR/SWIR FPAs and Applications
Tara J. Martin, UTC Aerospace Systems (United States)
Eric M. Costard, SOFRADIR (France)
Andrew Hood, FLIR Electro-Optical Components (United States)

2 Tomorrow's Systems Enabled by Today's Advanced Technologies
Mario O. Münzberg, Cassidian Optronics GmbH (Germany)
Torbjorn Skauli, Norwegian Defence Research Establishment (Norway)

3 Technologies for Advanced Applications
John L. Miller, FLIR Systems, Inc. (United States)

4 Type II Superlattice FPAs I
Meimei Tidrow, U.S. Army Night Vision & Electronic Sensors Directorate (United States)
Manijeh Razeghi, Northwestern University (United States)
Lucy Zheng, Institute for Defense Analyses (United States)

5 Keynote Session
Bjorn F. Andresen, Senso Optics Ltd. (Israel)

6 Type II Superlattice FPAs II
Meimei Tidrow, U.S. Army Night Vision & Electronic Sensors Directorate (United States)
Manijeh Razeghi, Northwestern University (United States)
Lucy Zheng, Institute for Defense Analyses (United States)

7 Advances in Optical and Detector Materials
Lucy Zheng, Institute for Defense Analyses (United States)
Troy A. Palmer, StingRay Optics, LLC (United States)

8 HOT: High Operating Temperature FPAs
Michael T. Eismann, Air Force Research Laboratory (United States)
Philip Klipstein, SCD Semiconductor Devices (Israel)

9 Uncooled FPAs and Applications
Masafumi Kimata, Ritsumeikan University (Japan)
Chuan C. Li, DRS Technologies, Inc. (United States)

10 Emerging Uncooled Technologies
Colin E. Reese, U.S. Army Night Vision & Electronic Sensors Directorate (United States)
Kevin C. Liddiard, Electro-optic Sensor Design (Australia)
Charles M. Hanson, Texas Instruments Inc. (United States)

11 ROIC
Paul L. McCarley, Air Force Research Laboratory (United States)
John T. Caulfield, Cyan Systems (United States)

12 IR Optics I: Technologies and Design
Christopher C. Alexay, StingRay Optics, LLC (United States)
Jay N. Vizgaitis, U.S. Army Night Vision & Electronic Sensors Directorate (United States)

13 IR Optics II: Breakthroughs in Multiband Moldable Glasses
Jay N. Vizgaitis, U.S. Army Night Vision & Electronic Sensors Directorate (United States)
Christopher C. Alexay, StingRay Optics, LLC (United States)
Shyam S. Bayya, U.S. Naval Research Lab. (United States)

14 IR Optics III: Multiband IR-GRIN Lenses
Jay N. Vizgaitis, U.S. Army Night Vision & Electronic Sensors Directorate (United States)
Christopher C. Alexay, StingRay Optics, LLC (United States)
Shyam S. Bayya, U.S. Naval Research Laboratory (United States)

15 Emerging Cryogenic Coolers
Alexander Veprik, SCD Semiconductor Devices (Israel)
Ingo Rühlich, AIM INFRAROT-MODULE GmbH (Germany)
Richard Rawlings, DRS Technologies, Inc. (United States)

16 Cryogenic Coolers
Alexander Veprik, SCD Semiconductor Devices (Israel)
Ingo Rühlich, AIM INFRAROT-MODULE GmbH (Germany)
Richard Rawlings, DRS Technologies, Inc. (United States)

17 HgCdTe
Joseph G. Pellegrino, U.S. Army Night Vision & Electronic Sensors Directorate (United States)
David Billon-Lanfrey, SOFRADIR (France)

18 HgCdTe: Reducing the Pitch
Ronald G. Driggers, St. Johns Optical Systems (United States)

19 QWIP and Q-DOT
Henk Martijn, IRnova AB (Sweden)

20 Smart Processing
Paul L. McCarley, Air Force Research Laboratory (United States)
John T. Caulfield, Cyan Systems (United States)

21 Face Recognition
Brian E. Lemoff, West Virginia High Technology Consortium Foundation (United States)

Introduction

The Fortieth conference on Infrared Technology and Applications was held the week of May 4th-8th, 2014 at the Baltimore Convention Center in Baltimore, Maryland. The agenda was divided into 21 sessions:

1. NIR/SWIR FPAs and Applications
2. Tomorrow's Systems Enabled by Today's Advanced Technologies
3. Technologies for Advanced Applications
4. Type II Superlattice FPAs I
5. Keynote Session
6. Type II Superlattice FPAs II
7. Advances in Optical and Detector Materials
8. HOT: High Operating Temperature FPAs
9. Uncooled FPAs and Applications I
10. Emerging Uncooled Technologies I
11. ROIC
12. IR Optics I: Technologies and Design
13. IR Optics II: Breakthroughs in Multiband Moldable Glasses
14. IR Optics III: Multiband IR-GRIN Lenses
15. Emerging Cryogenic Coolers
16. Cryogenic Coolers
17. HgCdTe
18. HgCdTe: Reducing the Pitch
19. QWIP and Q-DOT
20. Smart Processing
21. Face Recognition

In addition, there were twenty-five poster papers presented for discussion on Tuesday evening—these have been added to the 21 sessions in the Proceedings. Highlights of six topical areas are summarized below:

- Photon Detectors
- Uncooled Detectors
- Optics
- Coolers
- Smart Processing
- Applications

Photon Detectors

NIR/SWIR FPAs and Applications

Near-infrared and shortwave infrared imaging—0.7 to 3 μm—continues to rise in popularity because of its ability to make use of sky glow to enhance performance during exceptionally dark periods of the night.

Development of SWIR FPAs is continuing in order to meet the needs of both military and commercial applications. Most of these developments make use of InGaAs, although new SWIR HgCdTe (MCT) FPAs are also being developed for applications that require longer cutoff wavelength—above 1.7 μm.

Pixel sizes of InGaAs FPAs are decreasing. Two companies reported on their 12.5 μm pitch 1280 × 1024 InGaAs FPAs. As the pixels get smaller surface leakage current must be controlled in order to keep the dark current low. One company did this with a proprietary dielectric passivation as shown in Fig.1.

The other major source of dark current, junction diffusion current, was controlled by operating at an optimum bias voltage. The result was a total dark current of 0.7 nA/cm^2 at an operating temperature of 15 ºC or 2.0 nA/cm^2 at an operating temperature of 20 ºC.

Another company described its 1280 × 1024 and 640 × 512 InGaAs FPAs with 12.5 μm pixels and efforts to decrease total camera operating power. Rather than eliminating the thermo-electric cooler (TEC) com-

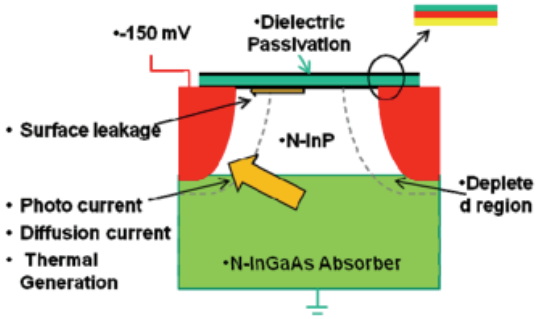

Fig. 1 Planar InGaAs/InP pixel structure used to fabricate 1280 × 1024 InGaAs FPA.

pletely, the company retained the TEC but used several temperature setpoints in order to reduce the TEC power. The result for a 640 × 480 camera is that power consumption remains below 2 W across a wide operating range, rising to 3 W at the extreme ends of the temperature range (-40 ºC and +80 ºC). This allows battery lifetimes of 6 hours or more using just three CR123A cells.

In another presentation, a 640 × 512 pixel, 20 μm pitch, InGaAs array was liquid nitrogen cooled for electroluminescence studies and astronomical applications. Total dark noise was only 5 electrons per pixel.

Two companies presented their results on MCT SWIR FPAs. One company grew high performance low cost MCT SWIR FPAs by MBE on 3" CdTe-buffered silicon substrates. Despite the large lattice mismatch between HgCdTe and Si substrate, the materials and detector performance are better than those reported for III-V mixed crystals. High minority carrier lifetime and low dark current densities were measured. Quantum efficiency exceeding 70% at 2.0 μm, without antireflective coating, was measured on single element detectors. FPAs were fabricated with this HgCdTe on Si material and imaging and radiometric characterization performed from 77K through room temperature.

Another company described their MCT SWIR FPAs (0.85 to 1.75 μm) that were grown lattice-matched on in-house fabricated CdZnTe substrates by a Liquid Phase Epitaxy (LPE) dipping process. 640×512 FPAs with 15 μm pixel pitch were processed in planar diode technology with n-on-p polarity. The company has adapted its high operating temperatures (HOT) technology that was developed for MWIR detectors SWIR detectors.

The measured dark current densities are less than one order of magnitude within the values of the empirical Rule 07 for MCT detectors with a cut-off wavelength of 1.75 μm. Thus, at an operating temperature of 240 K the measured dark current density is 2 nA/cm^2. (A dark current density of 1 nA/cm^2 or less is assumed to be required for applications under airglow.)

A comparison of the quantum efficiencies of 640 × 512 SWIR MCT FPAs with 15 μm pitch (at 210 K) and InGaAs FPAs at room temperature are shown in Fig. 2.

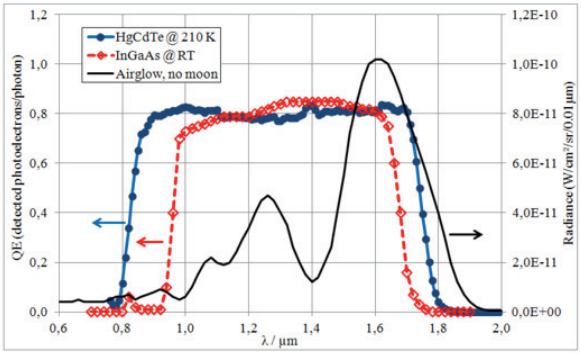

Fig. 2 Comparison of quantum efficiencies of InGaAs at room temperature and HgCdTe at 210 K.

For NIR applications, silicon-based imagers are continuing to be improved. In particular, CMOS imagers are used in a wide variety of applications, including large numbers of cell phone cameras which are replacing standalone digital cameras and are also starting to replace video camcorders due to the availability of low cost solid state memory and high quality miniaturized optics.

CMOS sensors have also demonstrated performance unachievable by any other semiconductor imaging array in high end TV, cinematography, slow motion and low light level cameras, thus revolutionizing digital image capture in general.

However, the adoption of CMOS sensors in space and astronomy instruments has been slow. Many new remote sensing systems and telescopes are still being equipped with CCDs, although, for longer exposure time applications, science CMOS image sensors (sCMOS), have gained wide acceptance in remote sensing, biological imaging, and machine vision.

There may be two reasons why CMOS sensors have not found their way into these applications more frequently: (1) the high cost of space based systems or large telescopes which can lead designers to use field-proven solutions to minimize risk and avoid cost escalation and (2) the fact that state-of-the-art CMOS sensors are highly optimized for images visible to the human eye rather than in the NIR or UV that are critically important for scientific applications.

One of the presentations describes a backside illuminated CMOS image fabricated on high resistivity silicon. The use of a thick photosensitive membrane allows carrier depletion with low background doping concentration while maintaining low dark current and good MTF performance. A 640 × 512 sensor was shown to have high quantum efficiency over a wide spectral range and a fast photodetector response.

Type II Superlattice FPAs

There were a total of eleven papers in the two sessions devoted to Type II Superlattice and Barrier detectors, and several more on this subject in the Poster session. This reflects the continued strong interest in the potential performance advantages that this technology has been predicted to have theoretically—long carrier lifetimes and a high optical absorption coefficient. Experimentally, lifetimes as long as those predicted have not yet been achieved, but improvements have been made recently for material structures that exclude gallium. Lifetimes continue to be shorter than for HgCdTe with comparable bandgaps.

Using InAs/InAsSb superlattices, and avoiding Ga to achieve longer lifetime, LWIR and VLWIR FPAs were reported. Quantum efficiency was reduced however, compared with Ga-containing structures, with LWIR values about 18 % in the 8-10 μm region, but higher in the MWIR band. VLWIR D* was about 10^{10} Jones.

LWIR InAs/GaSb superlattices were reported. Homojunction and hetrojunction designs were compared. Fig. 3 shows the dark current vs. bias and the photoresponse vs. bias for the designs measured. Dark currents in the low 10^{-4} A/cm^2 were achieved for a 10 μm cutoff bandgap.

InAs/GaSb Type II superlattice pB_np barrier devices were reported that were designed using a modified **k • p** model. This paper also confirms the lower quantum efficiency of Ga-free alloys. For cutoff wavelengths in the range of 9.2 to 9.9 μm, the dark current is within about a factor of 10 of HgCdTe rule 07 as shown in Fig. 4.

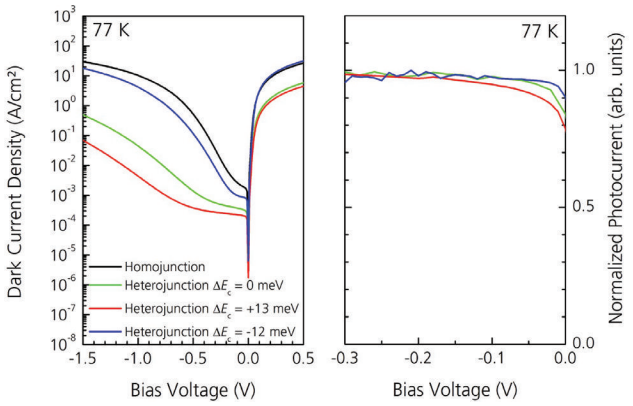

Fig. 3 Dark current density and photocurrent as a function of bias for homo- and hetro-junction Type II LWIR superlattice structures.

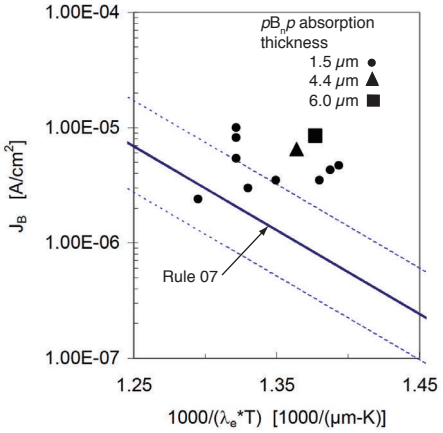

Fig. 4 Comparions of dark current density values for serveral InAs/GaSb pB_np absorption layer thickness designs with HgCdTe Rule 07.

Bi-spectral, MWIR/MWIR Type II superlattice FPA performance was updated showing the impact of improved passivation in reduced high-noise tails in the histograms of NEΔT values—see Fig. 5. Improvements are attributed to better passivation technology. This update covers results from a production program for a threat warning application.

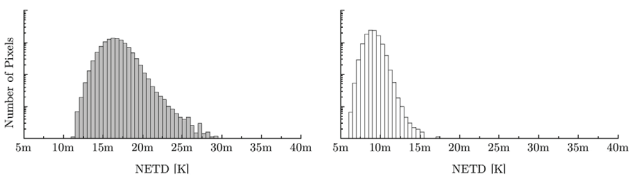

Fig. 5 NEΔT histograms with reduced high-noise tails from an ongoing MWIR/MWIR InAs/GaSb production program for a threat warning application.

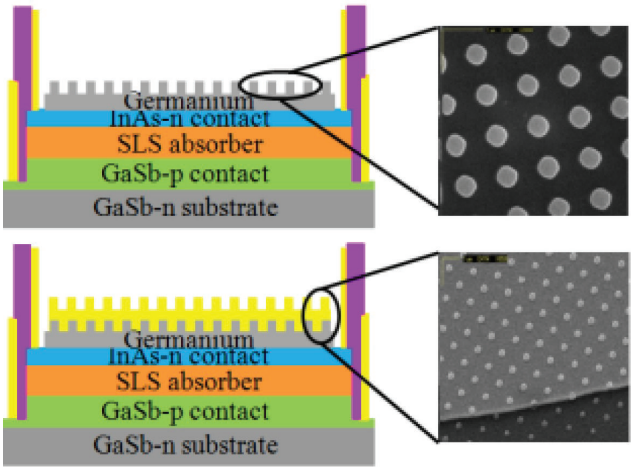

Fig. 6 A plasmonic coupler is fabricated on top of an MWIR Type II superlattice detector using a combination of germanium and gold.

MWIR InAs/GaSb superlattice *pin* photodiodes were evaluated for dark current, quantum efficiency, and the angular photo-response.

In another paper, MWIR InAs/GaSb superlattice detectors were combined with a plasmonic coupler to enhance the quantum efficiency. Fig. 6 illustrates how the plasmonic couplers were integrated into the structure.

Papers were presented discussing surface passivation of Type II superlattices with a nitrogen plasma and with ZnTe. Figure 7 compares the effectiveness of a variety of passivation methods in suppressing dark current in small diodes. Chlorine-doped ZnTe appears to be a promising candidate.

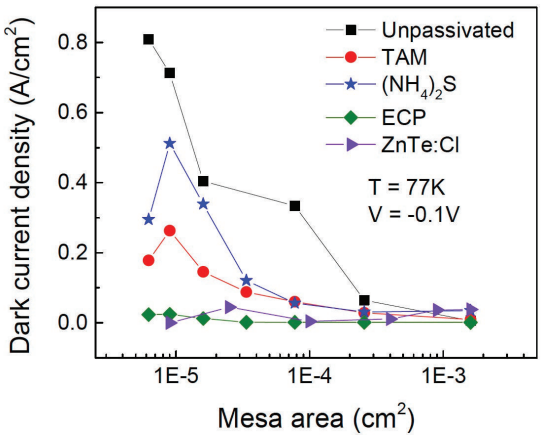

Fig. 7 ZnTe:Cl and ECP provided the lowest dark current for small mesa diodes.

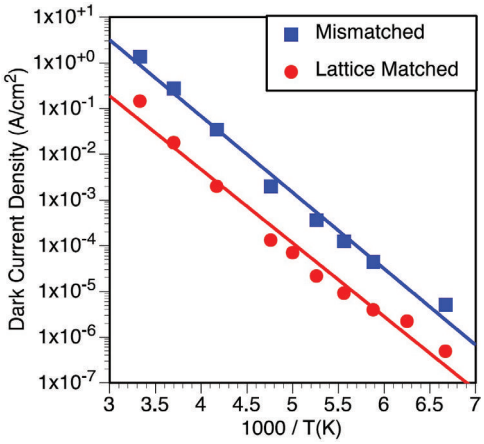

Fig. 6 Lattice-matched InAs *nBn* devices show about an order of magnitude lower dark current than those on lattice mismatched substrates.

InAs *pn* photodiodes and *nBn* detectors were compared on lattice-matched substrates and on mismatched substrates. Fig. 8 shows the dark current vs. inverse temperature for the case of *nBn* devices. Lattice matching yields about an order of magnitude dark current reduction.

MWIR Type II superlattice detectors having an 'N' structure were described. The InAs-GaSb absorber layers incorporated an asymmetric AlSb barrier that the authors claim increases absorption and decreases dark current.

A model was presented for an ideal InAs *nBn* detector where the barrier layer is doped n-type and where the dark current is assumed to be only due to Auger-1 and radiative recombination. The model gives guidance for maximizing photocurrent and avoiding depletion regions.

Barrier detectors were compared to HgCdTe photodiodes, especially with respect to high operating temperature performance. Fig. 9 a) and b) show the comparison that was presented for the MWIR and LWIR bands (5 and 10 μm cutoff values). In spite of the many attractive features of the III-V materials, their dark current densities are higher than that of HgCdTe. To increase their competitive position, improvements in lifetime, passivation, and hetrostructure engineering are needed.

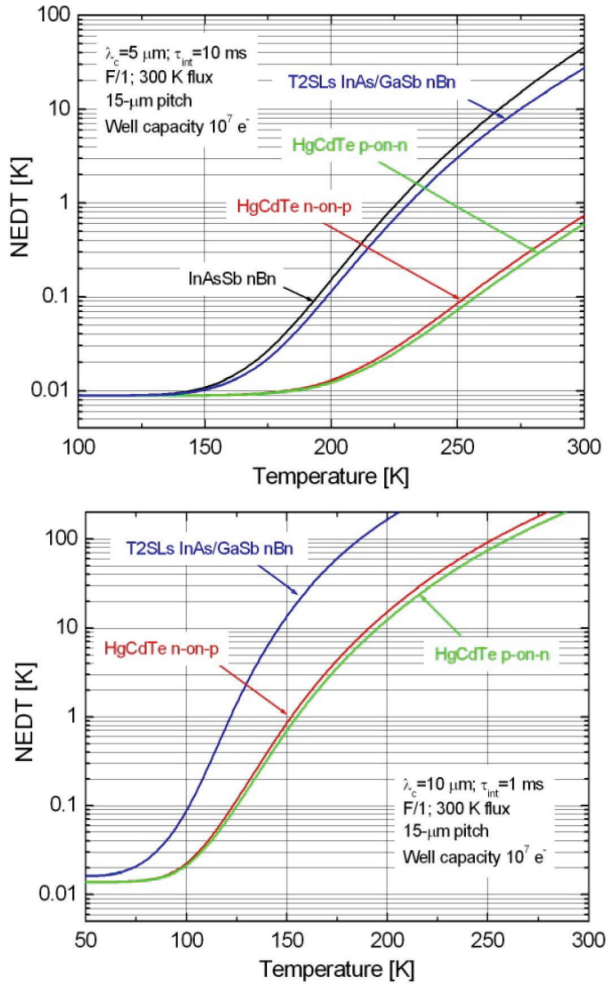

Fig. 9 A comparison of NEΔT values for 5 μm cutoff MWIR (top) and 10 μm cutoff LWIR (bottom) for barrier detectors and HgCdTe photodiodes.

Advances in Detector Materials

The trend towards ever-larger FPAs for astronomy and other applications has led to the development of larger infrared crystal materials. A paper announced the recent development of 5- and 6-inch InSb crystals. Fig. 10 shows the progression of InSb crystal size.

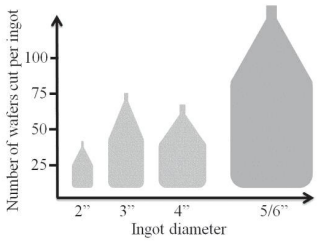

Fig. 10 Progression of InSb crystal size and the number of wafers that can be cut from them.

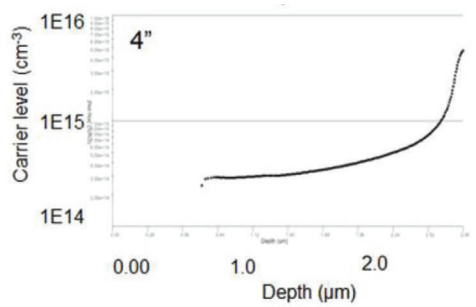

Fig. 11 Carrier concentration depth profile from a 2.5 μm thick InGaAs layer grown on a 4-inch InP substrate.

SWIR detectors using InGaAs are also endeavoring to increase production capacities, in this case by MOVPE growth on multiple 4-inch InP wafers in a single run. One measure of the success of this approach is the carrier concentration depth profile shown in Fig. 11.

High Operating Temperature (HOT) FPAs

The goal of increasing the operating temperature of FPAs without sacrificing performance is motivated by the reduction in cooler power, improved cooler efficiency, longer cooler lifetime, smaller imager size, and lighter weight sensor systems that this makes possible. This goal is being pursued using HgCdTe, Type II superlattices, and *nBn* materials and has relevance especially in the MWIR and LWIR spectral bands.

Efforts to increase the operating temperature of HOT MWIR HgCdTe detectors while also reducing the number of defective pixels were summarized in one paper. Fig. 12 shows the increase in temperature at which the dark current and photocurrent become

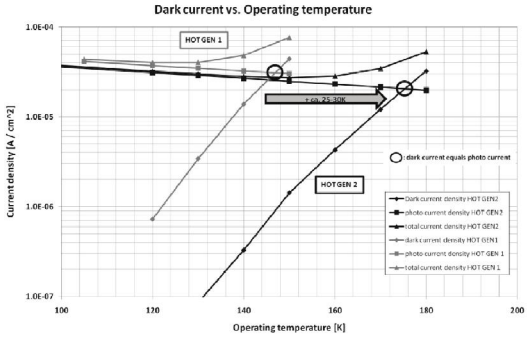

Fig. 12 Progress in raising the temperature at which dark current equals photocurrent is illustrated.

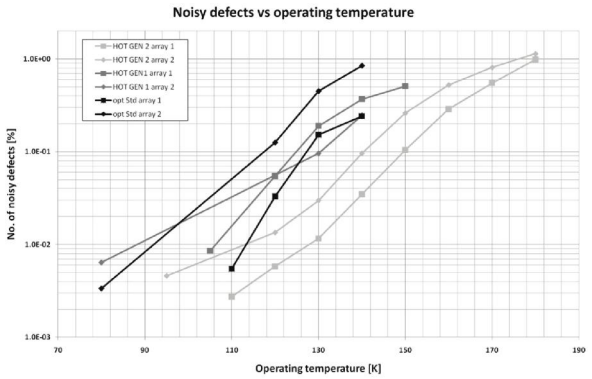

Fig. 13 Progress in raising the temperature at which them number of defective pixels increase.

equal, while Fig. 13 illustrates the corresponding temperature dependence in defective pixel count.

Another paper reported increases in HOT performance of HgCdTe MWIR FPAs. Fig. 14 shows how the NEΔT distribution at 155 K with f/4 flux was tightened in the past two years, reducing the high noise tail that reflects the number of defective pixels. Fig. 15 shows imagery at three elevated temperatures—at 217 K the cooling power was less than 1 W.

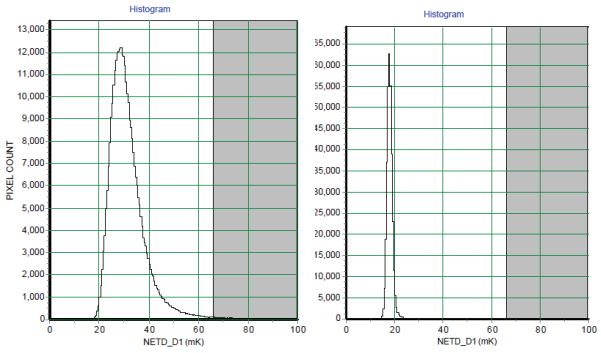

Fig. 14 Reduction in the high-noise tail in an MWIR HgCdTe NEΔT histogram over the past two years.

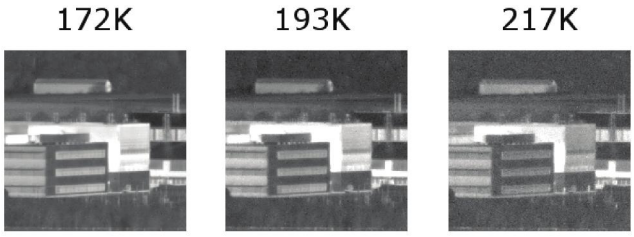

Fig. 15 Infrared imagery from an MWIR HgCdTe FPA at three elevated temperatures.

XBn III-V InAsSb barrier detectors are being developed for HOT applications. One of these has a spectral range from 3.4 to 4.2 μm and operates at 150 K. A larger format—1280 × 1024—with 15 μm pixels was described. Fig. 16 shows the integrated detector-cooler package.

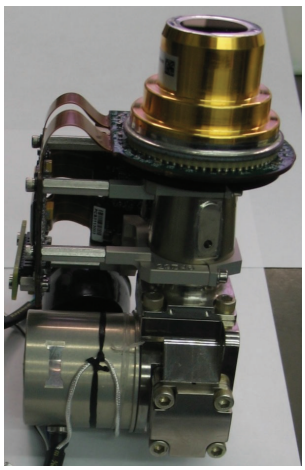

Fig. 16 Integrated detector-cooler package for a large-format XBn InAsSb barrier detector.

The absorption coefficient of Type II superlattice materials was the subject of a detailed study. It has been observed that Ga-free materials have longer carrier lifetimes than Ga-containing constituents. The absorption coefficient of a Ga-free MWIR superlattice at 160 K was compared to that of InSb at 80 K as shown in Fig. 17. The superlattice exhibits a softer spectral cutoff compared to direct bandgap alloy materials.

Monolithic PbSe FPAs operating at 230 K with an NEΔT of 30 mK, f/1 at 400 Hz were reported. Imagery was shown—see Fig. 18. Pixel operability was over 99.5% for a 240 × 320 array having 60 μm pixels. This PbSe technology is an MWIR photon detector with a potential cost of production that compares favorably to uncooled microbolometers. Typical spectral D* values for PbSe are shown in Fig. 19.

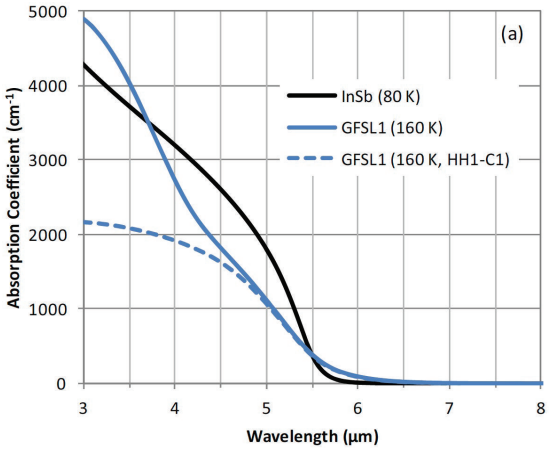

Fig. 17 Optical absorption coefficient comparison between InSb and two Ga-free Type II superlattice designs.

Fig. 18 30 mK infrared imagery from an MWIR PbSe FPA at 230 K and 400 frames per second.

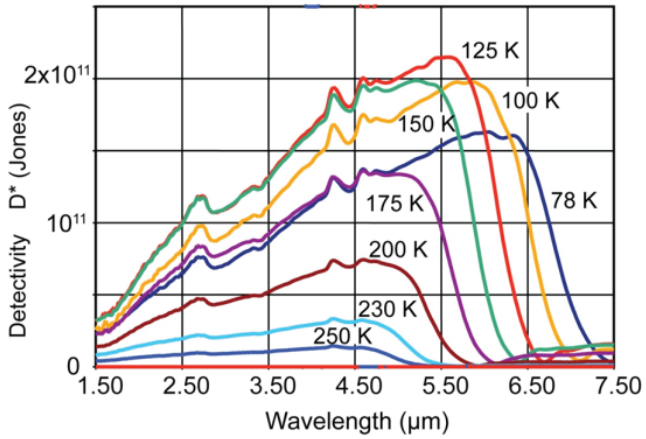

Fig. 19 Spectral D* for PbSe at temperatures between 250 and 78 K. The D* decreases at temperatures below 125 K because the spectral response is increasing—consult a theoretical D* vs wavelength chart..

HgCdTe

The HgCdTe alloy detector—characterized by a high absorption coefficient and a long lifetime—continues to dominate the choice for a broad range of infrared applications. Aside from applications that are ideal for either InSb in the MWIR spectral band, or InGaAs in the 1.7 μm SWIR band, or those that can utilize uncooled FPAs, HgCdTe continues to be the most popular choice. Papers in this section update how HgCdTe is continuing to develop and evolve. Papers on this topic were presented in two sessions on HgCdTe detectors as well as in the HOT session, the Applications sessions, and in the Poster session.

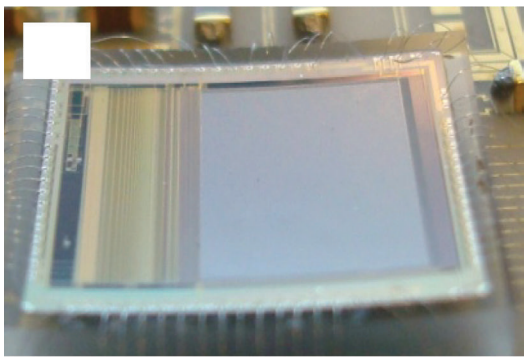

Fig. 20 An uncooled FPA that has been spherically shaped to make more efficient use of optics designs.

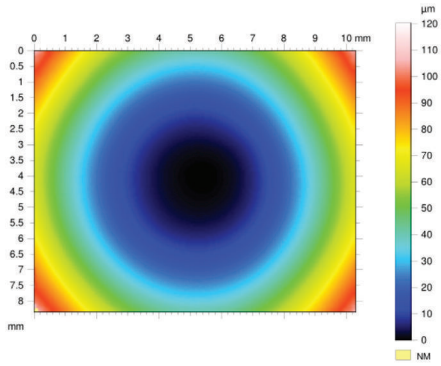

Fig. 21 Interference fringes showing the uniformity of curvature for a HgCdTe cooled FPA hybrid.

An exciting paper was presented in which spherically-curved FPAs—both cooled HgCdTe and uncooled—were fabricated and tested. Fig. 20 shows the uncooled FPA after it was spherically shaped. Fig. 21 shows the interference pattern from a cooled HgCdTe FPA. Curved FPAs allow for optics designs that are more efficient. Detector properties were little-changed after the process. Improved MTF was illustrated for one particular design comparison.

HgCdTe FPA developments for astronomy and spectroscopy were described, as well for SWIR avalanche photodiodes. Electron-avalanche devices were reported for MOVPE grown devices that have separate absorption and avalanche regions. Fig. 22 shows the excess noise figure for an e-APD. Single-photon detection was reported. Large format arrays of 1032 × 1280 with 15 μm pitch having a source-follower per detector, and a 1048 × 2056 with 17 μm pitch have been made. Also described was an extended-range—2.5 to 10 μm—FPA capable of 1000 frames per second for an imaging Fourier spectrometer.

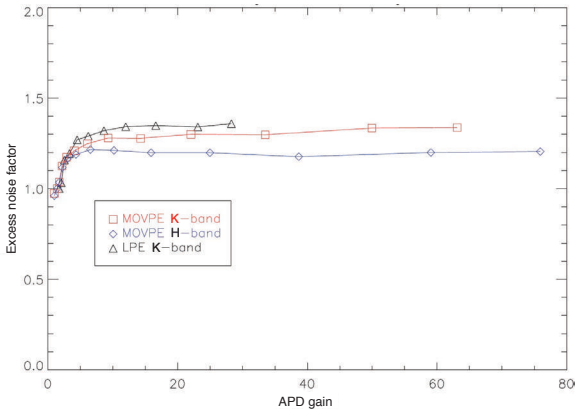

Fig. 22 Excess noise factors compared for LPE- and MOVPE-grown e-APDs.

New threats are prompting a push to higher resolution and larger format HgCdTe FPAs using MBE growth on GaAs substrates. A progression of FPAs has been proposed as follows:

Year	Format	Pitch (μm)
present	640 × 512	15
2015	1024 × 768	10
2020	1440 × 1080	7
2025	2048 × 1536	5

The pixel size is envisioned to shrink as the format goes up in proportion to maintain the use of the same dewar package. Fig. 23 shows an array of 10 μm pixels in proportion to a human hair.

Improvements in the performance and reliability of MWIR and LWIR HgCdTe detectors was described for n-on-p diodes. Among other things, the improved

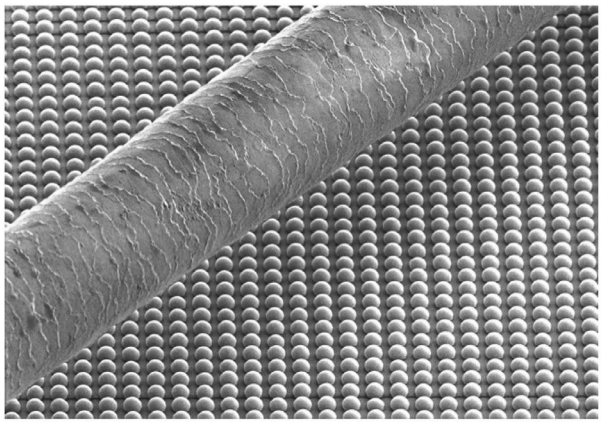

Fig. 23 An array of 10 μm HgCdTe pixels in comparison to a human hair.

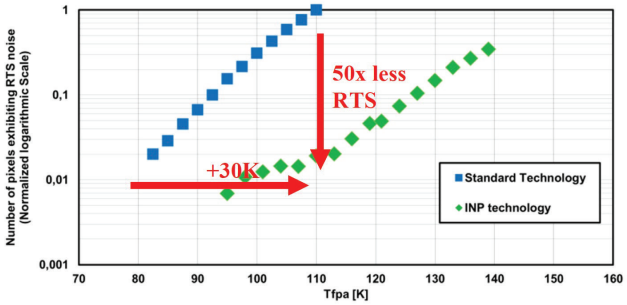

Fig. 24 The number of pixels showing random telegraph noise as a function of temperature for standard- and improved- n-on-p MWIR diodes.

diodes—INP—showed much reduced random telegraph (also called popcorn or burst) noise. Fig. 24 shows the 50 × impact of the improved process on this phenomena. Device stability up to 15,000 hours was documented.

Compact plasmonic metal-insulator-metal (MIM) metamaterial antenna designs for MWIR and LWIR bands were proposed in combination with HgCdTe absorbers.

HgCdTe p-on-n detector technology with extrinsic In- and As-doping has enabled R_0A performance to approach Rule 07 over a broad range of cutoff wavelengths in the LWIR-to-VLWIR range. Fig. 25 shows the improvements compared to earlier n-on-p devices. A variety of SWIR diode results were also reported in this paper.

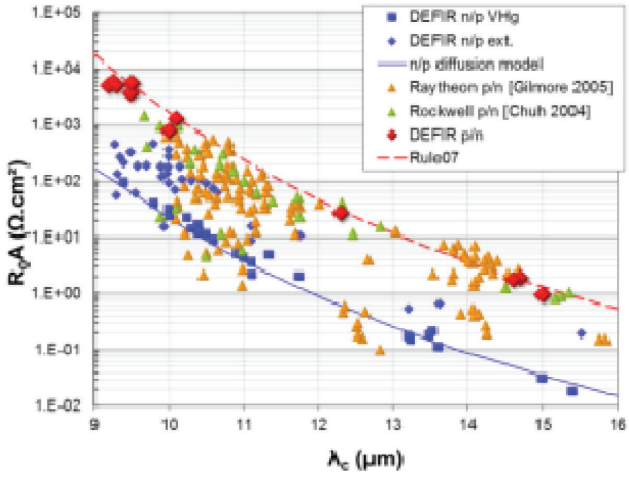

Fig. 25 Improved p-on-n technology has enabled an increase in HgCdTe R_0A values approaching Rule 07 over a wide range of LWIR-to-VLWIR cutoff wavelengths.

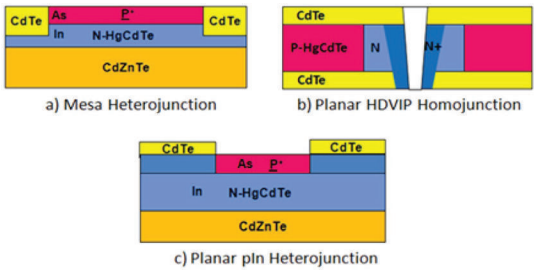

Fig. 26 Candidate pixel designs for small pitch: a) mesa p^+n, b) HDVIP or Loophole, c) planar-implanted junction *pIn*.

Reducing the pitch

.

Smaller pitch HgCdTe FPAs was the topic of one session. The challenges associated with obtaining small pitch— ~5 μm —were outlined, including:

- pixel delineation
- pixel hybridization
- unit cell well-capacity
- dark current

Fig. 26 above shows candidate device structures. The goal is to also include operation at temperatures as high as room temperature. As part of this examination, one other detector material and device technology were compared to HgCdTe diodes varieties:

- InAsSb alloy *nBn*; N = 10^{16}/cm^3; τ_{SR} = 400 ns.
- HgCdTe N^+/P hetero-junction; P = 3×10^{15}/cm^3; τ_{SR} = 4 ms.
- HgCdTe $N^+/N^-/P$ HDVIP homojunction; P = 2×10^{16}/cm^3; τ_{SR} = 4 ms.
- HgCdTe planar P^+/N hetero-junction; N = 4×10^{14}/cm^3; τ_{SR} = 4 ms.
- HgCdTe planar $P^+/n^-/N^+$ pIn; N = 2×10^{14}/cm^3; τ_{SR} = 4 ms.

An example of the dark current predicted is illustrated in Fig. 27.

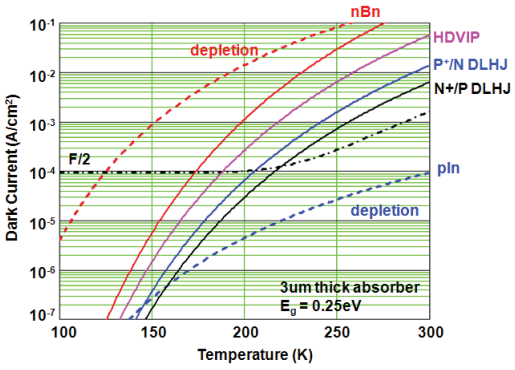

Fig. 27 Modeled dark currents for five candidate detector material and structures between 100 and 300 K.

Fig. 28 LWIR image taken with a 720 × 1280 FPA having 5 μm pixels. An f/1 lens was used.

In a follow-up paper, the results of imaging with 5 μm pitch FPAs was presented. This was done with an HDVIP pixel structure. Fig. 28 shows an image from a 720 × 1280 FPA with 5 μm pixels. Quantum efficiency was reported to be 45-55 % and LWIR operability was 99.6 %.

10 μm pitch FPAs in two formats—720 × 1280 and 768 × 1024—were announced for the MWIR band. Selectable charge storage was used to adjust the gain ranges from 0.7- to 4.4 × 10^6 electrons, together with a dynamic range of 80 dB. Fig. 29 shows NEΔT and operability as a function of temperature. Future consideration is being given to image dithering to effectively provide 5 μm pixel resolution with 10 μm pixels.

The benefits of small pixels were illustrated in a paper that first noted the significant reduction in false alarm rates that is possible because a true alarm will create a point-spread function blur in a group of pixels while a noise spike is likely to be confined to a

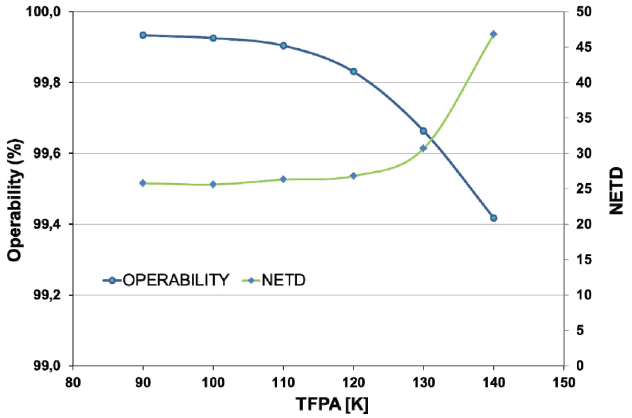

Fig. 29 NEΔT and operability for an MWIR FPA having 10 μm pixels as a function of operating temperature.

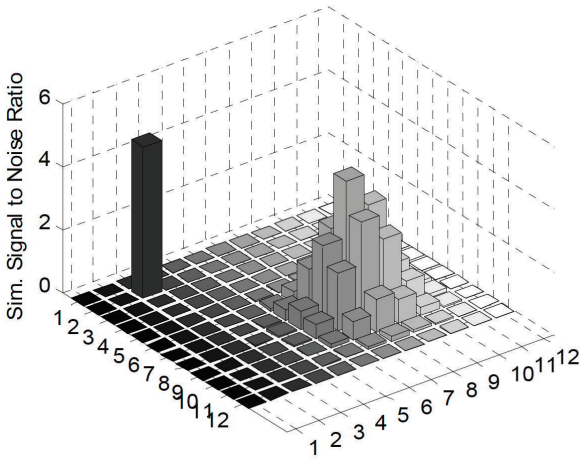

Fig. 30 An over-sampled true-alarm signal will produce a group of pixels from the signal point-spread function while a noise spike will only be generated in a single pixel.

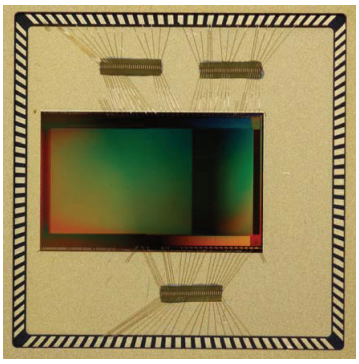

Fig. 31 A 2 Mpixel ROIC having 5 μm pixels and featuring on-chip correlation and noise reduction.

single pixel. Fig. 30 illustrates this concept. The paper also described the development of a readout with a 2 Mpixel format of 5 μm pixels designed to provide correlation and noise reduction directly in the readout. Fig. 31 shows a photo of the readout.

Another paper on this general topic of small pixels considered the implications of pixel reduction on the modulation transfer function—MTF. Experimental measurements were compared to results from finite element modeling so that a variety of general mitigation factors could be considered. Fig. 32 compares experimental data and the model for two pixel sizes and for a variation of diffusion lengths. The impact of surface recombination and crystal potential fields were also considered along with mesa etch depth.

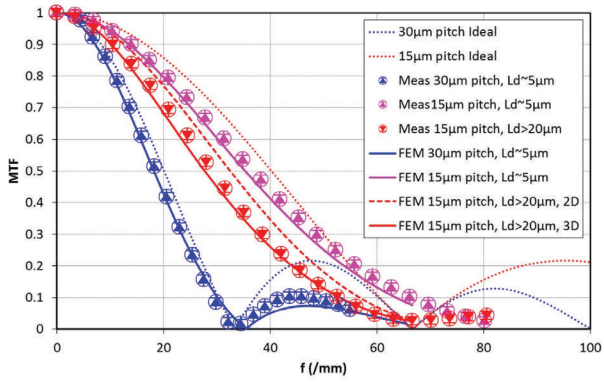

Fig. 32 MTF measurements for 30- and 15 μm pixels having several values of lateral collection length compared to calculations from a finite element model.

QWIP and Q-Dot FPAs

Quantum well and dot structures were discussed in three papers at the conference. In the first of these, an optical ring resonator was considered for boosting QWIP quantum efficiency. A variety of designs were modeled, followed by some experimental verification. Peak quantum efficiency of 30 % was achieved together with about 10 % collection efficiency. Higher values of quantum efficiency were modeled, but the model showed that there was a trend towards lower quantum efficiency with smaller pixels as shown in Fig. 33. A 640 × 512 FPA was demonstrated.

A second paper explored plasmonic structures to enhance quantum dot detectors—one design had narrow spectral response while another had a broader band response.

Colloidal PbS quantum dot devices were studied as a possible low-cost SWIR detector.

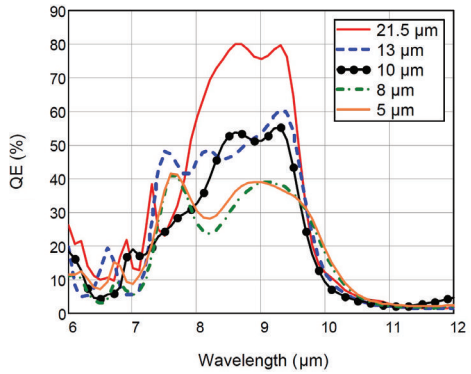

Fig. 33 Quantum efficiency as a function of wavelength for LWIR resonator-QWIPs with five different pixel sizes.

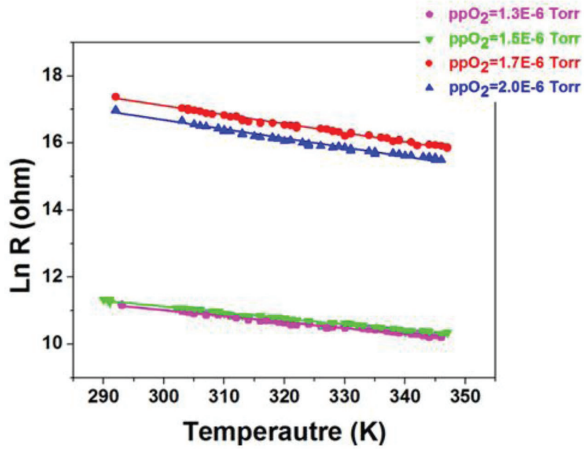

Fig. 34 The natural logarithm of MoO_x resistance prepared at different ppO_2 decreases linearly with increasing of temperature.

Uncooled Detectors

Emerging Uncooled

While microbolometers based on VO_x and α-Si have shown remarkable resilience against changes in market requirements for both performance and cost, there remains considerable interest in finding better ways to sense infrared radiation. Activities include new materials, more efficient absorbers, and innovative concepts. A U.S. university is investigating both nickel oxide and molybdenum oxide as materials having potential for improved process controllability by virtue of reduced sensitivity to the partial pressure of oxygen during material deposition. Molybdenum in particular is remarkable for the fact that the natural logarithm of its resistance varies linearly with temperature, as shown in Fig. 34, implying that its TCR is nearly constant with temperature.

In developments in Japan, an asymmetric plasmonic structure has been shown provide wavelength and polarization selectivity of absorption.

A paper presented by a U.S. university described analysis and experiment that verified the existence of a repulsive electrostatic force sufficient to overcome the Casimir force, which is the source of the "stiction" problem in MEMS devices. That permits fabrication of a unique null-switching infrared detector having inherently digital output. In a poster paper they also analyzed the effect of thermo-mechanical noise on this

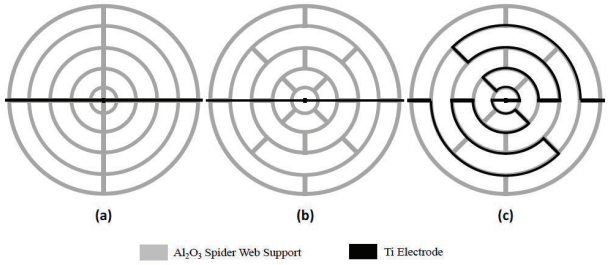

Fig. 35 Top view of the three designs used for simulation (a) Device 1: simple circular spider web with linear electrodes, (b) Device 2: meandered circular spider web with linear electrodes, and (c) Device 3: meandered circular spider web with meander electrodes.

detector. In this device a bi-material cantilever initially makes contact with an electrode on the substrate. A repulsive electrostatic force is suddenly activated, which moves the cantilever away from the substrate. A clock is then activated, and the applied voltage is ramped downward. The number of clock cycles until the cantilever again contacts the electrode is a measure of the radiation absorbed by the cantilever. The thermodynamic oscillation of the cantilever, primarily at its resonant frequency, is the dominant noise source.

An interesting approach by another U.S. university to achieve very high thermal isolation includes a web-like structure such as that shown in Fig. 35. The balanced mechanical design potentially permits long thermal conduction paths using nano-scale structures. So far, the effort has been limited to analysis, and the structures contemplated are large relative to state-of-the art bolometers. Nevertheless, it represents another arrow in the quiver of the pixel designer.

In a very unusual approach in Germany, devices have been fabricated based on what is believed to be the operating mode of infrared receptors in the *Melanophila acuminata* jewel beetle. A micro chamber between two silicon wafers contains a fluid that expands upon absorption of infrared radiation, and in doing so moves one plate of a capacitor. A narrow channel connects the chamber to a reservoir, providing a high-pass filter that eliminates spurious response to gradual ambient temperature changes.

A South Korean institute has demonstrated films of $VO_x/ZnO/VO_x$ with a TCR of -3.12 % and a resistance

of about 80 kΩ/square in a structure of 60 nm VO_x, 10 nm ZnO and 10 nm VO_x. The constituent films were deposited at room temperature, and the composite structure was annealed at 300 °C in oxygen.

A poster paper from Japan presented the results of a design study of 3-dimensional plasmonic infrared absorbers comprising a 2-dimensional array of micropatch antennas on posts that elevated them 150 nm above a bottom plate of the same material, gold. They found that the absorption was sharply peaked at a wavelength approximately proportional to the size of the micropatches, and that it was more sharply peaked if they were square rather than round. While the studied design included a relatively thick 200 nm bottom plate, it can be thinned significantly because of the small skin depth in gold. This technology is intended to enable detectors arrays wherein interspersed subarrays respond to different sub-bands of the IR spectrum. Along similar lines, a poster paper from Turkey showed enhanced absorption by using a planar array of plasmonic structures on the absorber.

A poster paper from a small U.S. business and a university presented results for a bolometer array using gold-doped VO_x, which lowered resistivity while maintaining a respectable TCR. Measured detector performance equates to a system NEΔT of less than 100 mK.

Uncooled

Uncooled IR microbolometer arrays continue to find application in many and varied places. Advancements include reductions in cost as well as improvements in performance, and the factors being addressed include packaging, readouts, pixel design and fabrication, and materials quality. Papers in the Uncooled FPAs and Applications session and the poster session were concerned with all these issues.

A new family of 17 μm microbolometer arrays from Germany includes a 640 × 480 version and a previously introduced 320 × 240 version, both incorporating massively parallel 16-bit sigma-delta ADCs located under the active array. The average $f/1$ NEΔT for those arrays is around 70 mK for a 30 Hz frame rate. The arrays are packaged chip scale; i.e., the array die

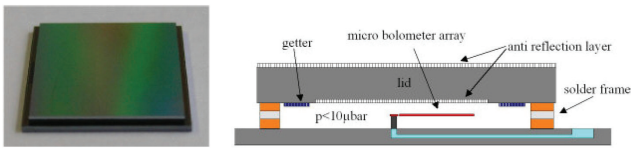

Fig. 36 Realization (left) and principle (right) of a chip-scale vacuum package.

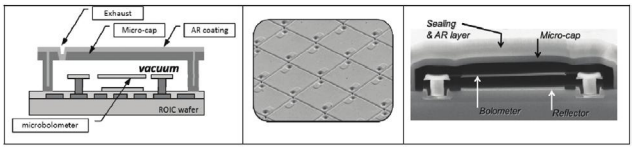

Fig. 37 Pixel-level packaging: left—schematic; center—SEM top view; right—SEM cross section.

are covered with an IR-transparent window separated from the array by a solder frame, as show in Fig. 36.

The development of pixel-level packaging for very low-cost sensors continues to progress in France. Fig. 37 shows such a device. The pixels of a microbolometer array are individually sealed by depositing an IR-transparent silicon film on top of a second sacrificial layer. Small holes in the silicon film facilitate the release etch, and the holes are afterward plugged by deposition of an anti-reflection coating. An 80 × 80 demonstration array indicates the initial package vacuum supports $f/1$ NEΔT in the range of 70 mK and pixel operability of 99.7 %.

Another approach to low-cost sensors is in development in Turkey—see Fig. 38. It uses bulk micromachining for more rigorous compatibility with a standard CMOS process, sacrificing sensitivity in the interest of substantial cost reductions. A standard met-

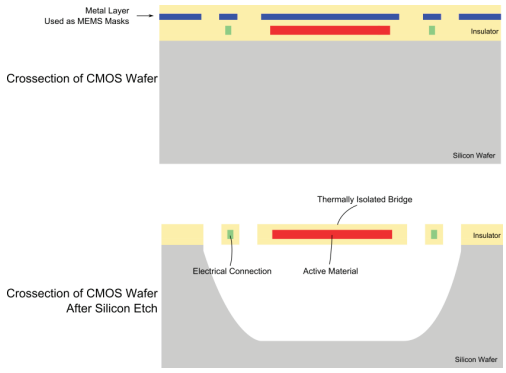

Fig. 38 Illustration of an ideal fabrication process as only one mask process step is required and no deposition step is used since the CMOS devices are used as the temperature sensing active material. The silicon beneath the detector bridge is etched in order to thermally isolate the detector bridge.

al layer serves as the mask for etching away silicon to release the bolometer structure. The sensor under development is a 160 × 120 array of 70 μm pixels operating at 30 Hz. The device power dissipation is 50 mW with analog output, and it is packaged at the wafer level. The f/1 NETD is less than 350 mK in a 1.65-in^3, 15-gram camera dissipating 625 mW.

A U.S. university is investigating the tradeoffs of resistance, TCR and 1/f noise in VO_x. The presence of 1/f noise in standard bolometric materials remains a limitation of bolometer technology. Increasing material resistivity generally increases TCR, but it also increases 1/f noise. The precise nature of the tradeoff is complex, because dynamic range, power dissipation and variability with ambient temperature also enter into the picture. The understanding is further complicated by the dependence of 1/f noise on the degree of crystallinity and the details of the deposition conditions.

The cost, performance, size and weight of uncooled IR sensors have made possible their implementation in smart munitions. A potentially serious impediment to their widespread use in such applications is the ability of the seemingly fragile pixel structures to withstand the excessive shock environments association with the firing and/or launching of munitions. A U.S. university has demonstrated that a microbolometer sensor, properly configured, can survive a 20,000-g shock and maintain it original performance.

In another development, a Canadian company has grown vanadium oxide films having nonuniformity of less than 2.5% rms across the entire 150 mm wafer, a four-fold improvement over previous results. This improvement was measured using a 4-point probe, and the results were confirmed using resistor bridge structures.

Optics

Four sessions were devoted to infrared optics – 3, 12, 13 and 14. Session 12 was focused on optical design while the three others discussed revolutionary developments in infrared materials – these are expected to have a strong influence on future designs.

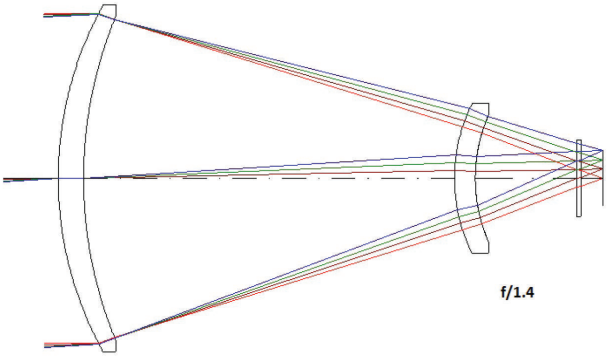

Fig. 39 A 100 mm f/1.4 LWIR lens.

The optical system design session addressed various ways to answer SWAP-C requirements. The cost, "C", of IR cameras is greatly reduced when the application allows for use of an uncooled microbolometer instead of a cooled photon detector. Responsibility for further cost reduction is now with the optics designer. One presentation discussed design for low-cost LWIR objectives for small pixels—see Fig. 39.

Reduction of size, "S", is another critical parameter for optical designers. One group developed a "flat" folded path LWIR lens for a microbolometer camera. The optical design uses four concentric aspheric mirrors—see Fig. 40. The 50 mm f/1.5 lens has an amazing 15 mm long optical train and a 5 mm back focal distance – small enough to fit within a 3" diameter ball gimbal.

Size was also one of the main concerns of a company which presented the optical design of a compact multiband imager integrated with a laser range finder. Imaging in the Visible and SWIR bands were achieved with two cameras employing a common zoom optical system that was also shared with the LRF receiver—see Fig. 41. The purpose of the sensor suite was day-

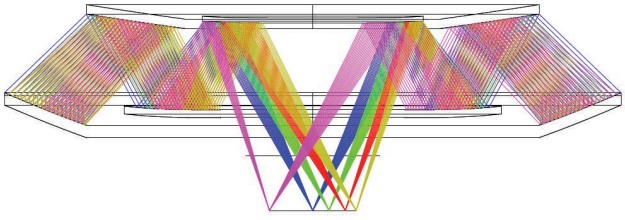

Fig. 40 Layout of a 50 mm f/1.5 LWIR four-folded reflective lens.

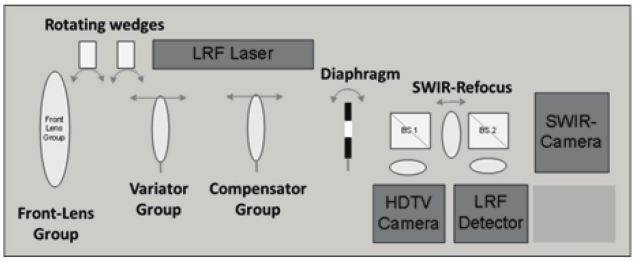

Fig. 41 Schematic layout of the multi-band sensor suite.

time long range target acquisition over sea in good and poor visibility conditions.

The optical and mechanical design challenges of a zoom system operating through a range of working distances while at the same time allowing a smoothly varying magnification range were discussed. The resulting elegant system is shown in Fig. 42..

A hyperspectral airborne pushbroom imaging spectrograph was presented in the applications session. Instead of using a pushbroom solution, one might consider an FPA combined with an electrically tunable narrow wavelength spectral filter having a msec response. Such a system would be less bulky and fragile. One research group presented a tunable reflective filter based on coupling plasmonic antenna arrays with liquid crystals—see Fig. 43 for an example of reflectance response.

Multispectral and hyperspectral systems are designed to increase target acquisition performance as well as to answer SWaP-C requirements for military and

Fig. 42 Finished zoom system without covers.

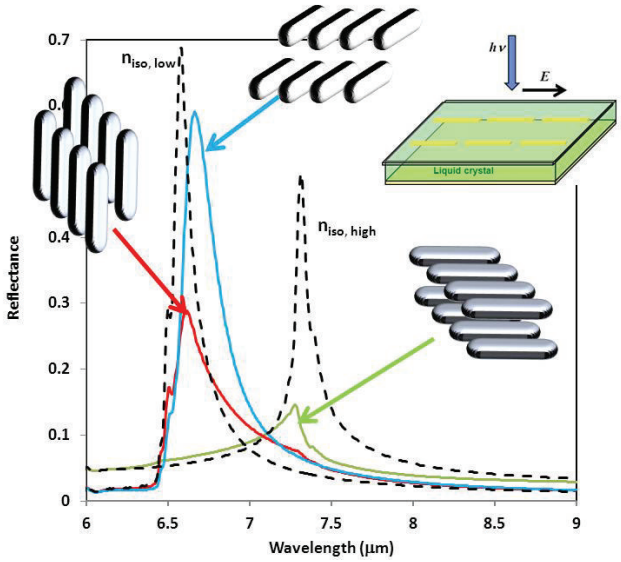

Fig. 43 Reflectance response of a nanobar antenna array to incident irradiation.

paramilitary systems. While today's FPAs can potentially enable compact, lightweight multiband spectral systems, there are few optical materials covering the SWIR – LWIR transmission range. The results of this is that several optical materials are needed to correct for chromatic aberrations over a broad wavelength spectrum – adding size and excessive weight to the systems.

Several laboratories presented results of their efforts to fill up the infrared glass map – closing the many gaps in the refractive index values. Foremost among these is the U.S. NRL. The Abbe numbers for their 13 new materials are shown in Fig. 44. In cooperation

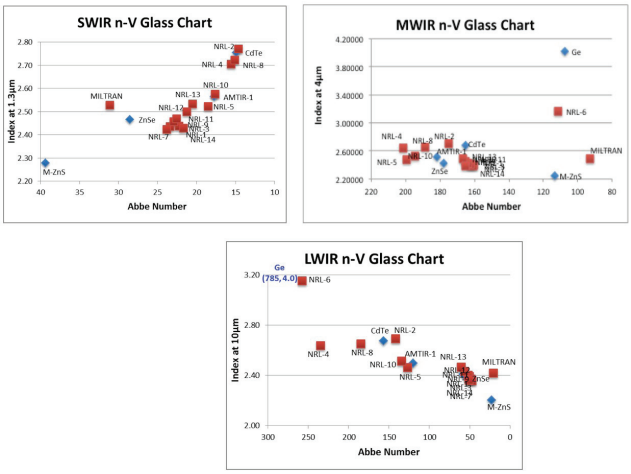

Fig. 44 NRL's new infrared glass map.

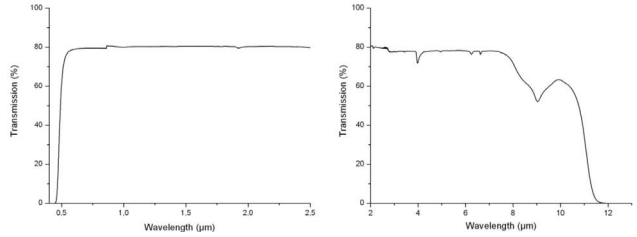

Fig. 45 Transmission of a new 4 mm thick Vis – LWIR sample.

with U.S. Army NVESD's optics group they demonstrated design examples showing the strong impact of the new glasses on cooled and uncooled systems. By substituting new glasses for the traditional crystal materials it was shown in one case that the number of elements could be reduced from 4 to 2!

A French group, led by the University of Rennes, has added CsCl to a binary GeS_2-Ga_2S_3 material system and achieved good transmission from Visible to LWIR—see Fig. 45. Inclusion of the Visible band is important for reducing system size and weight in UAV, handheld and head-mounted systems. The material is moldable and, therefore, much less costly than the polycrystalline Cleartran (ZnS).

A university group reported on their investigation of organic polymers as possible alternative to inorganic metal oxide, semiconductor, or chalcogenide-based materials for optical components. They demonstrated that sulfur copolymers, obtained by using an inverse vulcanization process, possess low absorption in Visible to MWIR spectral bands—see Fig. 46.

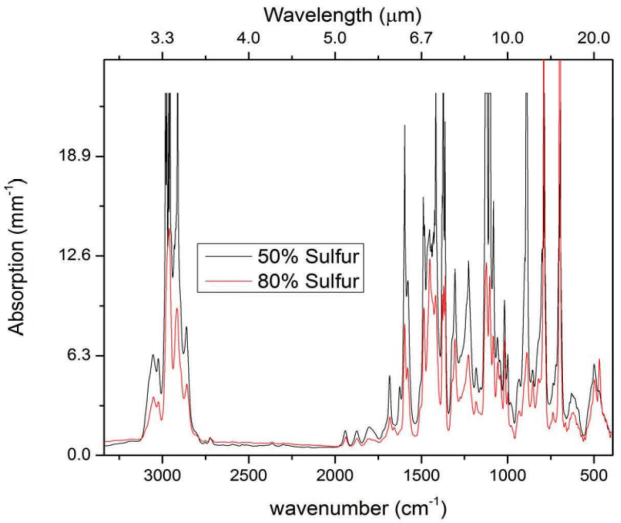

Fig. 46 Absorption spectra of 0.2 mm thick sulfur copolymers samples.

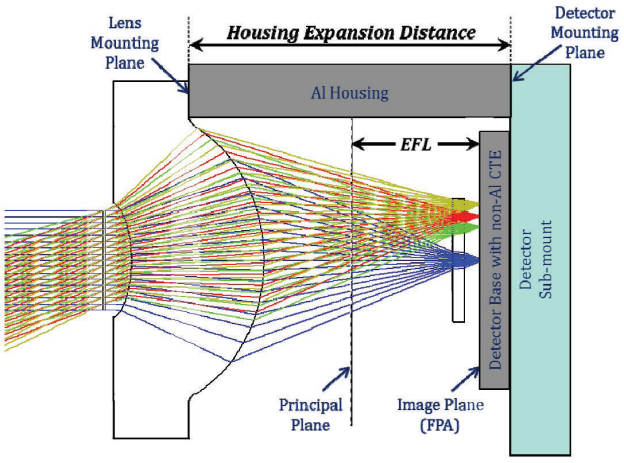

Fig. 47 Example of optomechanical layout

One company addressed the thermal effects on LWIR optical designs. A new athermal analysis methodology, which includes optomechanical considerations—see Fig. 47—was established. Following a comparison of the different lens materials, the advantages of chalcogenide materials were pointed out.

Coolers

The Cryocoolers for Infrared Detectors session was divided into two parts. The first part addressed emerging cryogenic cooler technologies and the second part discussed fine progress in the more "traditional" mechanical coolers.

Mechanical compressors and expanders, essential components of today's cryogenic coolers, are sources of audible noise and vibration export. They also cause limited life and awkward packing of the sensor system. Several laboratories are developing new and improving old non-mechanical technologies for cryogenic cooling. Among these are optical cooling, using fluorescence, and thermoelectricity (TEC).

One group, consisting of scientists from industry, university and the U.S. Air Force Res. Lab., explained the basic operation of optical cryocoolers. See illustration in Fig. 48. Fig. 49 shows how the cooling temperature depends critically on the class of materials used. The achieved cooling temperature of 93 K is already sufficiently low to cool all infrared detectors belonging to the HOT class.

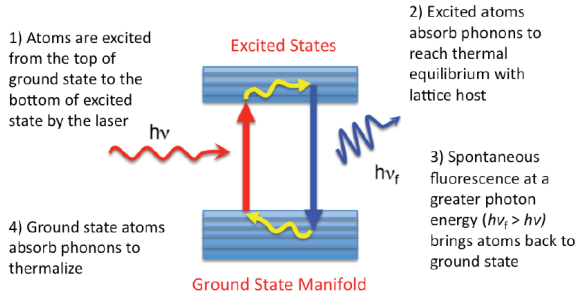

Fig. 48 Cooling cycle for optical refrigeration with rare-earth ions.

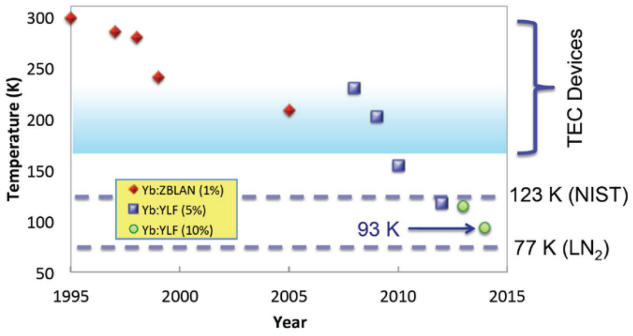

Fig. 49 Progress in optical refrigeration.

It should be noted that fine progress has been reported elsewhere for emerging cryogenic coolers based on the second technology—thermoelectricity (TEC). Cooling temperatures well below 170 K have been achieved using a superlattice structure material. Presentation of continued progress in both technologies are planned for SPIE's 2015 IRT&A conference.

While developers of the emerging technologies attempt to reach cooling temperatures as low as those required for today's HOT FPAs and beyond, manufacturers of mechanical cryo-coolers are aiming for cooling temperatures as high as those of HOT in order to improve the cooler's SWAP-characteristics. Low input power to the cooler is an important part of the SWAP requirements. The relation between power consumption and operating temperature is illustrated in Fig. 50.

Three companies addressed HOT mechanical cryo-coolers. They all discussed linear coolers while one also demonstrated rotary coolers. All reported cooling temperatures between 150 K and 160 K with 2 W DC power consumption.

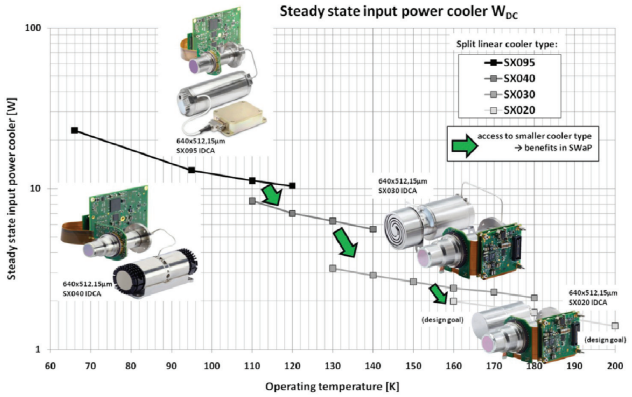

Fig. 50 Power consumption vs. cooling temperature for HOT-type mechanical cryocoolers.

In response to continuing requirements for smaller and lighter cryocoolers for tactical IR applications, one company demonstrated its smallest linear drive cooler for a micro-Integrated Dewar Cooler Assembly (μIDCA). The entire cooler / Dewar assembly occupies about 4 cubic inches. The design goals and constraints were presented and the resulting design discussed—see Fig. 51.

Among other important aspects of the mechanical cryo-coolers that were discussed are:

- Effective suppression of exported vibrations caused by motion of the free moving displacer of a Stirling cold finger.

- Development of special approaches to ruggedizing the sensitive components of cryogenically cooled infrared electro-optical payloads that are required to operate and survive frequent exposure to vibration and temperature extremes typical of the modern battlefield.

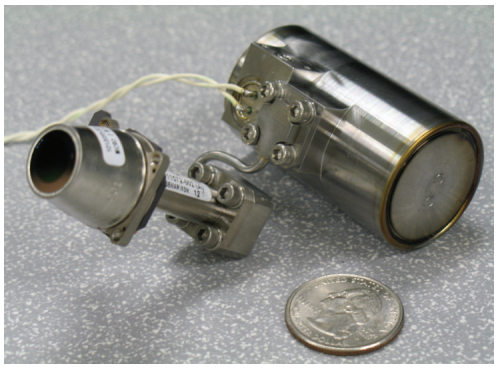

Fig. 51 One configuration of the μIDCA.

- Development of a family of high end digital cryo-cooler electronics which will address the widest possible range of aerospace infrared sensor applications.

- Improving reliability evaluation models for estimation of cryo-cooler reliability and MTTF.

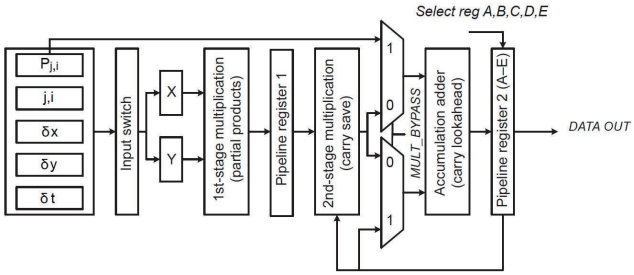

Fig. 53 Multiply-accumulate unit architecture.

Smart Processing

This session primarily covers advances in detector readout technology that include functionality beyond simple signal/image acquisition.

Fusion of visible and LWIR imagery was the subject of the first paper in this session, with an emphasis on minimizing latency. The steps that are necessary to enhance, align, rotate, parallax shift, and combine the visible and IR frames is described. Fig. 52 gives an example of the IR imagery contrast is enhanced. All steps are accomplished in less than 1 msec.

Digital readouts with digitization in the pixel have been a popular topic for several years now. One paper took this concept a step further, adding on-chip signal processing to enable low-latency—less than 10 μsec—implementation of functions for applications such as centroid trackers, Shack-Hartman wavefront sensors, and Fitts correlation trackers. The bandwidth of the outgoing data flow is reduced by as much as 80 % because the data hadt been preprocessed. Fig. 53 shows the unit architecture of the multiply-accumulate circuitry.

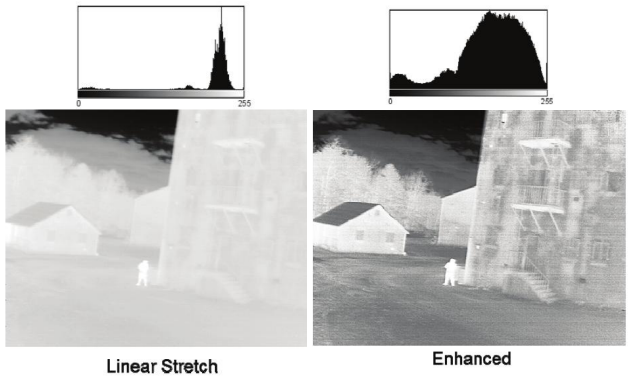

Fig. 52 IR imagery contrast is enhanced by cropping the signal histogram based on the previous frame.

One method for overcoming atmospheric turbulence distortion is to collect regions of image frames from so called "lucky frames" where the distortion happens to be minimal in a portion of the frame. The fusion of these regions gives an improved resolution image while sacrificing frame rate. Hardware implementation using parallel processing with field-programmable gate arrays—FPGAs—has enabled this approach to be accelerated.

Imaging with readouts that have computational capabilities on the FPA was reported. Two examples illustrated this concept, one for SWIR and one for visible. Fig. 54 shows the front and back of a camera built around the visible sensor.

A biologically-inspired infrared imager with on-chip object computation was described with a SWIR response. The chip has the capability for temporal and spatial processing and is being applied to detect pixel-level intensity changes and correlate them with nearby pixel changes. Fig. 55 shows a block diagram of the imager together with normal and reduced data output.

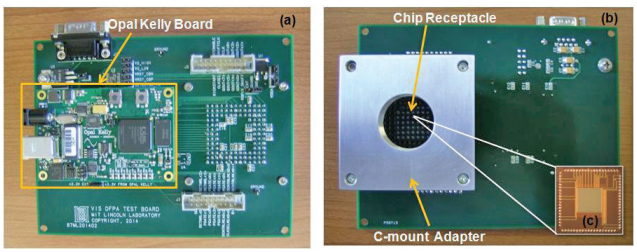

Fig. 54 Backside (a) and frontside (b) of the prototype computational camera. The array is seen in (c).

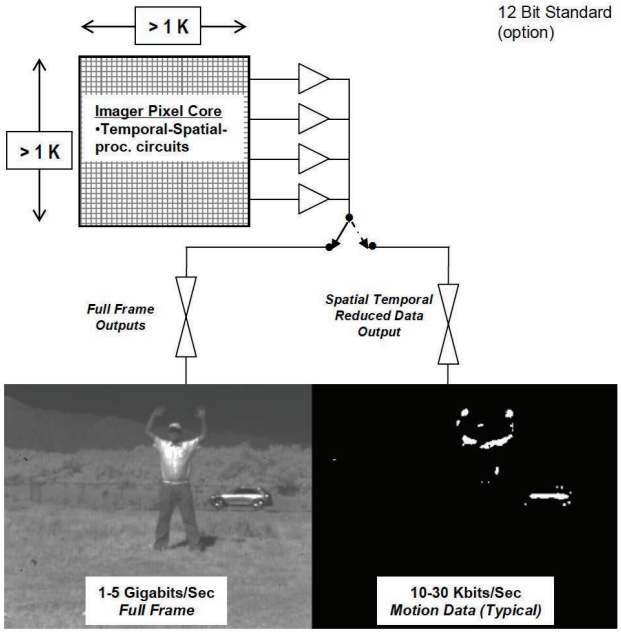

Fig. 55 Block functional diagram of dual mode SWIR imager with a normal video frame (left) and Spatial-Temporal reduced frame (right) using on sensor computation of intensity variations/ motion.

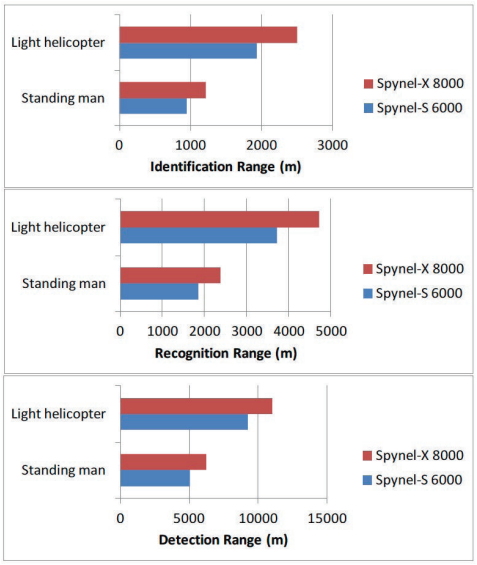

Fig. 56 360° IR imager detection, recognition, and identification ranges.

Applications

Presentations focusing on applications of the various infrared technologies in systems and subsystems were presented in Oral Sessions 2, 3, 21, and in the Poster Session. As applications are the main drivers for technology R&D, references to system applications can be found throughout the Proceedings.

The applications for panoramic imagers have multiplied during the last decade. Chief among them are IR Search and Track (IRST) warning sensor systems against aerial threats, perimeter security and situational awareness for autonomous vehicles.

Challenges and trade-offs involved in designing panoramic sensor systems were discussed. Use of a unique 360° lens design, stitching of three 120° sectors, and a continuously scanning solution were considered. One company presented their estimated target acquisition ranges for two slow 0.5 Hz frame rate, high spatial resolution scanning IRSTs—see Fig. 56.

Multi-spectral and hyper-spectral imaging is often used to support the process of target recognition at long ranges where the acquisition system's spatial resolution is insufficient.

A Norwegian and Canadian company have partnered in order to offer hyper- and multi-spectral solutions covering the entire visible to LWIR spectrum. The former company presented its NIR/SWIR airborne hyperspectral system delivering 6 nm spectral resolution based on transmission gratings. See system overview in Fig. 57.

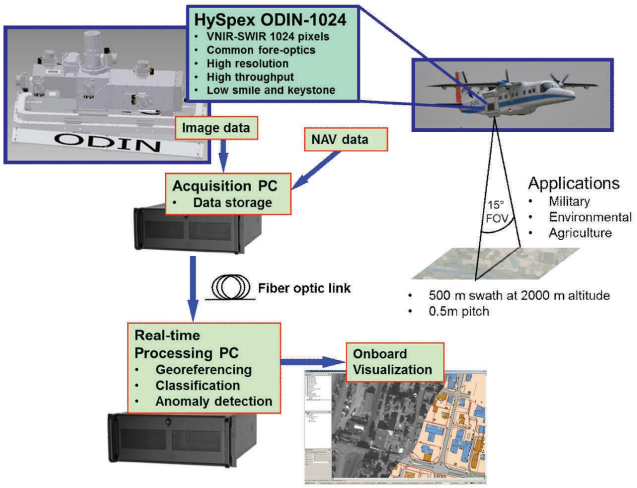

Fig. 57 Overview of airborne NIR/SWIR hyperspectral system.

Fig. 58 LW camera with filter wheel system

The Canadian LWIR multispectral system employs an 8-channel continuously rotating filterwheel—see Fig. 58. Examples of spectral investigation of chemical nature of gas and minerals where presented. Discrimination between signals due to emissivity and temperature differences were shown.

MWIR detectors based on HgCdTe and InSb materials, cooled to 77 K, with pixel counts up to 1280 × 1024 were discussed for applications ranging from satellite-borne cameras to missile seekers. For the latter application XBn-InAsSb and epi-InSb at higher temperatures enable faster cool-down and higher sensitivity. Uncooled microbolometers were considered for short and middle range missile seekers due to their lower cost and size and near-immediate readiness. Their increased sensitivity due to process modifications is illustrated in Fig. 59.

Thermal imagers having pixel counts varying between 1 and 1 million were presented. The one based on a single SWIR element made use of a tomographic scanner—claimed to the first operating in the IR region.

The mega-element MWIR imager was designed for border surveillance operation over long ranges. The high target acquisition performance was achieved by

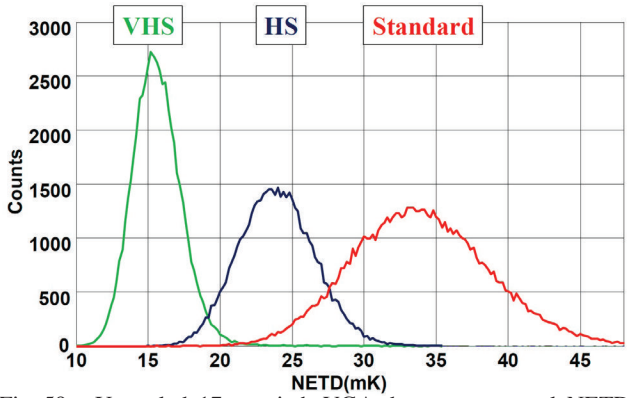

Fig. 59 Uncooled 17µm pitch VGA detector temporal NETD (F/1, 60Hz) of the VHS, HS, and Standard pixels.

Fig. 60 Example of atmospheric turbulence mitigation applied in central boxed region.

use of a small pixel size, a continuous zoom lens, and a novel turbulence mitigation algorithm—see Fig. 60.

Several other applications were demonstrated. Among them were

- A LWIR microbolometer which may be clipped on any smartphone for use in short range thermography or in defense / security scenarios. With one of a set of interchangeable lenses detection of a man at 500 m range was reported—see Fig. 61.

- Infrared imagery used forensically as evidence in court was demonstrated. The evidence supported police in prosecuting an in-

Fig. 61 Thermal imaging as a smartphone application.

Fig. 62 Example of thermal image (top), Google Street View image (middle), and colorized thermal image (bottom).

dividual for a crime where a conviction might not have been assured without the thermal information.

- Increasing night navigation safety by displaying the thermal image using, instead of false colors, a color map derived from a daytime reference image. The process was demonstrated by use of GPS and Google Street View—see Fig. 62.

Facial recognition plays a crucial role in many law enforcement scenarios. During the last decade many researchers have developed methods of face recognition based on reflective NIR and SWIR imaging.

Two groups presented results from their investigations into facial detection and recognition using the reflective parts of the IR spectrum. Irradiation of the face was used by both groups. One group made NIR tests at ranges up to 3 m. Algorithms for image preparation and face acquisition were discussed.

The other group developed an active SWIR imaging system enabling autonomous facial identification of moving subjects at distances above 100 m. Fusing of multiple images was found to be necessary for positive identification.

All infrared systems mentioned above may be incapacitated by a laser, or a strong flashlight or the sun irradiating the detector. The use of a designating laser to assist in target identification and tracking (See-Spot) can lead to transient dazzling or permanent damage of the sensor system. One company presented a novel passive threshold-triggered protection filter operating in the Visible to LWIR spectral region. The filter temporally blocks the damaging radiation while continuously transmitting the remaining scene.

Keynote address

The presentation-only keynote address discussed 1/f noise as possibly being a consequence of the turbulent flow of electronic charge—electronic gas. Central to this investigation is the question of whether the two standard equations of electron transport in semiconductors—drift and diffusion—should be supplemented by the Navier-Stokes equations that describe turbulent flow of gases and fluids. Clues about this idea originated with peculiar nature of the large difference in the strength of 1/f noise in HgCdTe depending upon whether the charge flow is relatively uniform such as from diffusion or photocurrent, or localized such as from GR centers or surface states that create small current jets—see Fig. 63. This difference in the strength of 1/f noise per unit of current has been confirmed to also occur for currents in silicon photodiodes. Theoretical calculations are being made to compare a

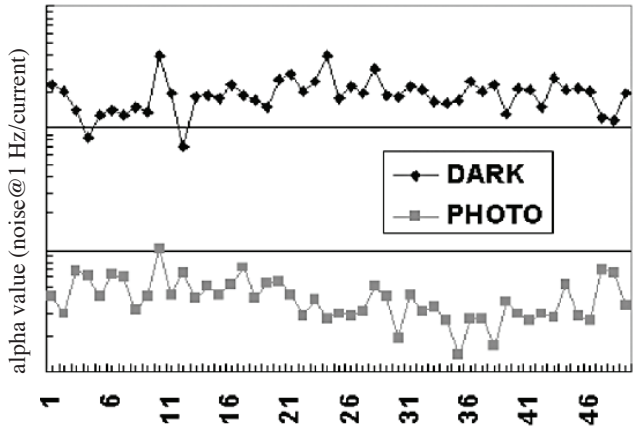

Fig. 63 Alpha values— a = noise@1 Hz/diode current—for a string of HgCdTe photodiodes at a fixed temperature. The induced photocurrent was much greater than the dark current.

Navier-Stokes model to predictions. Experiments to compare the data from Si and Ge photodiodes are also underway. Another test is suggested in Fig. 64 where it is postulated that the magnitude of 1/f noise will be greater in one of the two directions of bias voltage in a semiconducting structure.

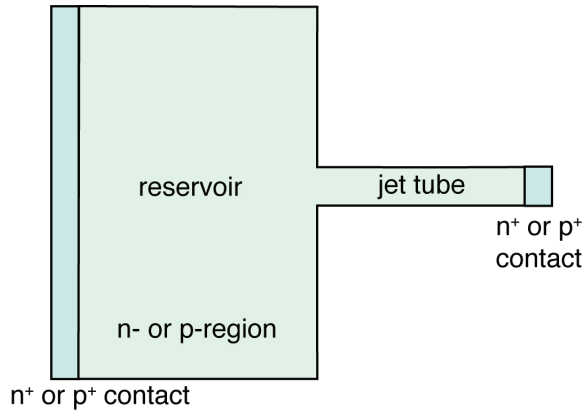

Fig. 64 1/f noise is predicted to be much greater for one bias direction compared to the other because one should be largely turbulent while the other should be mostly laminar.

40TH ANNIVERSARY OF INFRARED TECHNOLOGY AND APPLICATIONS

2014 was the 40th Anniversary of this conference. In August last year, Bjørn Andresen was presented with the SPIE Board of Directors award for his continuing stewardship. At our meeting in Baltimore, a cake was enjoyed by the attendees in honor of this anniversary.

40th Anniversary poster and cake to celebrate our Infrared Technology and Applications Conference!

Paul R. Norton

Bjørn F. Andresen

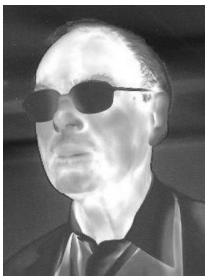

Gabor F. Fulop

Charles M. Hanson